AIAA 2002-5436

OPTIMAL CONTROL OF UNSTEADY FLOWS USING A TIME ACCURATE METHOD

Siva K. Nadarajah and Antony Jameson
Department of Aeronautics and Astronautics
Stanford University
Stanford, California 94305 U.S.A.

9th AIAA/ISSMO Symposium on Multidisciplinary Analysis and Optimization Conference
September 4–6, 2002/Atlanta, GA

AIAA 2002-5436

OPTIMAL CONTROL OF UNSTEADY FLOWS USING A TIME ACCURATE METHOD

Siva K. Nadarajah *and Antony Jameson †
Department of Aeronautics and Astronautics
Stanford University
Stanford, California 94305 U.S.A.

This paper presents an adjoint method for the optimal control of unsteady flows. The goal is to develop the continuous and discrete unsteady adjoint equations and their corresponding boundary conditions for the time accurate method. First, this paper presents the complete formulation of the time dependent optimal design problem. Second, we present the time accurate unsteady continuous and discrete adjoint equations. Third, we present results that demonstrate the application of the theory to a two-dimensional oscillating airfoil. The results are compared to a multipoint approach to illustrate the added benefit of performing full unsteady optimization.

Introduction

In the past decade, aerodynamic shape optimization has been the focus of attention due largely to advanced algorithms that have allowed researchers to calculate gradients cheaply and efficiently. The majority of work in this area have been focused on the design of aerospace vehicles in a steady flow environment. Investigators have applied these advanced design algorithms, particularly the adjoint method, to a vast number of problems, ranging from the design of two-dimensional airfoils to full aircraft configurations to decrease drag, increase range, and reduce sonic boom. These problems have been tackled using many different numerical schemes on both structured and unstructured grids. The reference sections in the following papers by Nadarajah et. al.[1,2] contains a list of papers by various different authors on the subject of aerodynamic shape optimization. This list by no means is comprehensive but should provide a reader who is interested in this research area a list of current efforts.

Unlike fixed wing aircrafts, helicopter rotors and turbomachinery blades are constantly subjected to unsteady loads. Therefore, optimal control of unsteady flows is essential to improving the performance of helicopter rotors and turbomachinery by reducing the unsteady effects that contribute towards flutter, buffeting, poor gust and acoustic response, and dynamic stall.

Helicopter Rotors. The flight envelope of a helicopter rotor is set by the compressibilities effects experienced by the advancing rotor blade and the retreating blade dynamic stall. As the helicopter forward flight speed is increased, the freestream velocity observed in the reference frame of the advancing blade is that of the sum of the helicopter forward flight speed and the speed of the advancing blade. At high cruise speeds, the freestream Mach number observed by the advancing blade reaches levels where local supersonic zones on the surface of the rotor blade are present. These regions usually terminate with a shock wave which causes a sudden increase in wave drag. During the retreating phase, the blade incidence approaches the stall angle, thus causing separation to occur on the upper surface of the blade which leads to a loss of lift.

At the 38th Cierva Memorial Lecture, Wilby[3] indicated that during the retreating blade stall it is the dramatic change in pitching moment more than the loss of lift that imposes a greater constraint on the design of the rotor blades. The change in pitching moment causes a large oscillatory load on the blade pitch control mechanism which reduces its fatigue life, thus increasing the operating cost of the helicopter. Over the years, researchers in the field of rotorcraft aerodynamics have developed ingenious methods to solve these problems. Their efforts have been focused on developing blade profiles that have a high maximum lift coefficient which allows the retreating blade to avoid stall incidence, low wave drag during the advancing phase, and low pitching moment to reduce blade twist and control loads. The introduction of the swept tip to reduce the wave drag and reflex camber towards

*Graduate Student, Student Member AIAA
†Thomas V. Jones Professor of Engineering, Stanford University, AIAA Fellow

the rear portion of the upper surface to increase negative loading thus reducing the pitching moment are just some of the technologies introduced over the last twenty years.

Turbomachinery. The flow through a turbomachine is highly nonlinear due to variation of the hub-to-tip distance along the blade row, blade-to-blade interference, and interactions between the rotors and stators. The presence of sources that generate nonlinear flow within the turbomachine have an unfavorable effect on the flutter characteristics of the blades. Researchers have developed blade profiles with good response to incoming gust and acoustic disturbances.

Diverse methods have been employed in the design of rotorcraft and turbomachinery blades. The following are a selected number of papers on this topic. Ghayour et. al.[5] solved the unsteady transonic small disturbance equation and its continuous adjoint equation to perform an inverse design at Mach 0.6. Aerodynamic shape optimization of rotor airfoils in an unsteady viscous flow was approached by Yee et. al.[6] using a response surface methodology. Here the authors used an upwind-biased-factorized implicit numerical scheme to solve the RANS equations with a Baldwin-Lomax turbulence model. A response surface methodology was then employed to optimize the rotor blade. The objective function was a sum of the L/D at three different azimuth angles and was later redefined to include unsteady aerodynamic effects. Florea et. al.[7] modeled a cascade of turbomachinery blades using the steady and time-linearized Euler equations. The gradients were then computed using the discrete adjoint approach. Both the flow and adjoint equations were solved using a finite-volume Lax-Wendroff scheme. Both aeroelastic and aeroacoustic objective functions were used to improve the aeroelastic stability and acoustic response of the airfoil.

Traditionally, a multipoint approach has been used for the optimization of blade profiles in an unsteady flow environment. This approach only requires a small extension of a researcher's steady flow design code in order to redesign a blade or airfoil profile. A typical multipoint design method requires the following three steps: First, steady flow solutions are computed for a various number of cases by varying freestream conditions. Second, the gradients for each case is computed using either a classical finite-difference method or using an adjoint approach. Third, the gradients are weighted and the blade profile is redesigned to satisfy the design objective.

In this paper, we develop a framework to perform sensitivity analysis in a nonlinear unsteady flow environment and to further modify the shape of the object to achieve the objective of the design using a full unsteady optimization method based on control theory. Optimal control of time dependent trajectories is generally complicated by the need to solve the adjoint equation in reverse time from a final boundary condition using information from the trajectory solution, which in turn depends on the control derived from the adjoint solution. In this work, we extend the adjoint method to unsteady periodic flows using a time accurate approach. The time accurate unsteady adjoint equations are based on Jameson's cell-centered multigrid-driven fully-implicit scheme with upwind-biased blended first and third order artificial dissipation fluxes.[4]

The goal of this research is to develop both the time-accurate continuous and discrete adjoint equations and use them in the redesign of the RAE 2822 and VR-7 rotor airfoils undergoing a pitching oscillation to achieve lower time-averaged drag while keeping the time-averaged lift constant. This technique is compared to a multipoint and steady adjoint approach to gauge the effectiveness of the method.

Governing Equations

In order to allow for geometric shape changes it is convenient to use a body fitted coordinate system, so that the computational domain is fixed. This requires the formulation of the Euler equations in a transformed coordinate system. The Cartesian coordinates and velocity components are denoted by x, y, and u, v. For a control volume Ω with a moving boundary $\partial\Omega$ and moving with Cartesian velocity components x_t and y_t, the equations of motion of the fluid can be written in integral form as

$$\frac{d}{dt}\iint_{\Omega}\mathbf{w}dxdy+\oint_{\partial\Omega}\left(\mathbf{f}dy-\mathbf{g}dx\right)=0, \qquad (1)$$

where the state vector $\mathbf{w}$, inviscid flux vector $\mathbf{f}$ and $\mathbf{g}$ are described respectively by

$$\mathbf{w}=\left\{\begin{array}{c}\rho\\ \rho u\\ \rho v\\ \rho E\end{array}\right\},\quad \mathbf{f}=\left\{\begin{array}{c}\rho\left(u-x_t\right)\\ \rho u\left(u-x_t\right)+p\\ \rho v\left(u-x_t\right)\\ \rho E\left(u-x_t\right)+pu\end{array}\right\},$$

$$\mathbf{g}=\left\{\begin{array}{c}\rho\left(v-y_t\right)\\ \rho u\left(v-y_t\right)\\ \rho v\left(v-y_t\right)+p\\ \rho E\left(v-y_t\right)+pv\end{array}\right\}. \qquad (2)$$

In these definitions, ρ is the density and E is the total energy. The pressure is determined by the equation of state

$$p=\left(\gamma-1\right)\rho\left\{E-\frac{1}{2}\left(u_iu_i\right)\right\}.$$

For discussion of real applications using a discretization on a body conforming structured mesh, it is also useful to consider a transformation to the computational coordinates (ξ_1,ξ_2) defined by the metrics

$$K_{ij}=\left[\frac{\partial x_i}{\partial\xi_j}\right],\quad J=\det\left(K\right),\quad K_{ij}^{-1}=\left[\frac{\partial\xi_i}{\partial x_j}\right].$$

The Euler equations can then be written in computational space as

$$\frac{\partial (Jw)}{\partial t} + \frac{\partial F_i}{\partial \xi_i} = 0 \quad \text{in } \mathcal{D}, \tag{3}$$

where the inviscid flux contributions are now defined with respect to the computational cell faces by $F_i = S_{ij} f_j$ and the quantity $S_{ij} = JK_{ij}^{-1}$ represents the projection of the ξ_i cell face along the x_j axis.

When equation (3) is formulated for each computational cell, a system of first-order ordinary differential equations is obtained. To eliminate odd-even decoupling of the solution and overshoots before and after shock waves, the conservative and viscous fluxes are added to a diffusion flux. The artificial dissipation scheme used in this research is a blended first and third order flux, first introduced by Jameson, Schmidt, and Turkel.[9] The artificial dissipation scheme is defined as

$$\begin{aligned} D_{i+\frac{1}{2},j} &= \epsilon^2_{i+\frac{1}{2},j}(w_{i+1,j} - w_{i,j}) \\ &\quad - \epsilon^4_{i+\frac{1}{2},j}(w_{i+2,j} - 3w_{i+1,j} + 3w_{i,j} - w_{i-1,j}). \end{aligned} \tag{4}$$

The first term in equation (4) is a first order scalar diffusion term, where $\epsilon^2_{i+\frac{1}{2},j}$ is scaled by the normalized second difference of the pressure and serves to damp oscillations around shock waves. $\epsilon^4_{i+\frac{1}{2},j}$ is the coefficient for the third derivative of the artificial dissipation flux. The coefficient is scaled so that it is zero at regions of large gradients, such as shock waves and eliminates odd-even decoupling elsewhere.

General Formulation of the Time-Dependent Optimal Design Problem

Optimal control of time dependent trajectories is generally complicated by the need to solve the adjoint equation in reverse time from a final boundary condition using data from the trajectory solution, which in turn depends on the control derived from the adjoint solution.

Introduce the cost function

$$I = \int_0^{t_f} \mathcal{L}(w, f)dt + \mathcal{M}(w(t_f)),$$

where the function $\mathcal{L}$ depends on the flow solution w, and the shape function f and the function $\mathcal{M}$ depends on the time dependent flow solution. Assume that the following equation defines the time-dependent flow solution

$$\frac{\partial w}{\partial t} + R(w, f) = 0,$$

where R represents a residue containing the convective and dissipative fluxes. A change in f results in a change

$$\delta I = \int_0^{t_f} \left(\frac{\partial \mathcal{L}^T}{\partial w}\delta w + \frac{\partial \mathcal{L}^T}{\partial f}\delta f \right) dt + \frac{\partial \mathcal{M}^T}{\partial w}\delta w(t_f), \tag{5}$$

in the cost function. The variation in the flow solution is

$$\frac{\partial}{\partial t}\delta w + \frac{\partial R}{\partial w}\delta w + \frac{\partial R}{\partial f}\delta f = 0. \tag{6}$$

Next, introduce a Lagrange multiplier ψ to the time-dependent flow equation, integrate it over time and subtract it from the variation of the cost function to arrive at the following equation.

$$\begin{aligned} \delta I &= \int_0^{t_f} \left(\frac{\partial \mathcal{L}^T}{\partial w}\delta w + \frac{\partial \mathcal{L}^T}{\partial f}\delta f \right) dt + \frac{\partial \mathcal{M}^T}{\partial w}\delta w(t_f) \\ &- \int_0^{t_f} \psi^T \left(\frac{\partial}{\partial t}\delta w + \frac{\partial R}{\partial w}\delta w + \frac{\partial R}{\partial f}\delta f \right) dt. \end{aligned} \tag{7}$$

By integrating the term $\int_0^{t_f} \psi^T \frac{\partial}{\partial t}\delta w dt$ by parts, yields

$$\begin{aligned} \delta I &= \int_0^{t_f} \left(\frac{\partial \mathcal{L}^T}{\partial w} + \frac{\partial \psi^T}{\partial t} - \psi^T \frac{\partial R}{\partial w} \right) \delta w dt \\ &+ \left(\frac{\partial \mathcal{M}^T}{\partial w} - \psi^T(t_f) \right) \delta w(t_f) \\ &+ \int_0^{t_f} \left(\frac{\partial \mathcal{L}^T}{\partial f} - \psi^T \frac{\partial R}{\partial f} \right) \delta f dt. \end{aligned}$$

Choose ψ to satisfy the adjoint equation

$$\frac{\partial \psi}{\partial t} = \left(\frac{\partial R}{\partial w} \right)^T \psi - \left(\frac{\partial \mathcal{L}}{\partial w} \right)$$

with the terminal boundary condition

$$\psi(t_f) = \frac{\partial \mathcal{M}}{\partial w}.$$

Then

$$\delta I = \mathcal{G}^T \delta f,$$

where

$$\mathcal{G}^{\mathcal{T}} = \int_0^{t_f} \left(\frac{\partial \mathcal{L}^T}{\partial f} - \psi^T \frac{\partial R}{\partial f} \right) dt.$$

The sensitivity derivatives are determined by the solution of the adjoint equation in reverse time from the terminal boundary condition and the time-dependent solution of the flow equation. These sensitivity derivatives are then used to get a direction of improvement and steps are taken until convergence is achieved.

The computational costs of unsteady optimization problems are directly proportional to the desired number of time steps. The unsteady flow calculation can be obtained either by the use of implicit time-stepping schemes or a non-linear frequency domain approach.

Derivation of the Time Accurate Continuous Unsteady Adjoint Equations for the Euler Equations

To control the surface pressure by varying the airfoil shape, it is convenient to retain a fixed computational domain. Variations in the shape then result in corresponding variations in the mapping derivatives defined by K. The cost function for drag minimization is

$$\begin{aligned} I &= \int_0^{t_f} C_d \, dt = \int_0^{t_f} C_a \cos\alpha + C_n \sin\alpha \, dt \\ &= \frac{1}{\frac{1}{2}\gamma P_\infty M_\infty^2 \bar{c}} \int_0^{t_f}\!\!\int_{\mathcal{B}} p \left(\frac{\partial y}{\partial \xi}\cos\alpha - \frac{\partial x}{\partial \xi}\sin\alpha \right) d\xi dt \end{aligned}$$

where C_a and C_n are the axial and normal force coefficients respectively. The design problem is now treated as a control problem where the control function is the airfoil shape, which is chosen to minimize I subject to the constraints defined by the flow equations. A variation in the shape causes a variation δp in the pressure and consequently a variation in the cost function

$$\begin{aligned} \delta I &= \frac{1}{\frac{1}{2}\gamma P_\infty M_\infty^2 \bar{c}} \int_0^{t_f}\!\!\int_{\mathcal{B}} \delta p \left[\frac{\partial y}{\partial \xi}\cos\alpha - \frac{\partial x}{\partial \xi}\sin\alpha \right] \\ &\quad + p\left[\delta\left(\frac{\partial y}{\partial \xi}\right)\cos\alpha - \delta\left(\frac{\partial x}{\partial \xi}\right)\sin\alpha \right] d\xi dt \quad (8) \end{aligned}$$

Since p depends on w through the equation of state, the variation δp is determined from the variation δw. Define the time-dependent flow equation as

$$\frac{\partial w}{\partial t} + \frac{\partial F_k}{\partial \xi_k} = 0.$$

Define the Euler Jacobian matrices as

$$A_k = \frac{\partial f_k}{\partial w}, \quad C_k = S_{kl} A_l.$$

Then the variation in the flow solution can be written as

$$\frac{\partial}{\partial t}\delta w + \frac{\partial}{\partial \xi_k}\delta F_k = 0,$$

where

$$\delta F_k = C_k \delta w + \delta S_{kl} f_l.$$

Multiplying by a co-state vector ψ, also known as Lagrange Multiplier, and integrating over the domain and time produces

$$\int_0^{t_f}\!\!\int_{\mathcal{D}} \psi^T \left[\frac{\partial}{\partial t}\delta w + \frac{\partial}{\partial \xi_k}\left(C_k \delta w + \delta S_{kl} f_l\right) \right] d\mathcal{D} dt = 0.$$

Separate the equation into two terms and switch the integrals for the first term to yield

$$\begin{aligned} &\int_{\mathcal{D}}\int_0^{t_f} \psi^T \frac{\partial}{\partial t}\delta w \, dt \, d\mathcal{D} \\ &+ \int_0^{t_f}\!\!\int_{\mathcal{D}} \psi^T \frac{\partial}{\partial \xi_k}\left(C_k \delta w + \delta S_{kl} f_l\right) d\mathcal{D} dt = 0. \end{aligned}$$

If ψ is differentiable, then the equation can be integrated by parts to give

$$\begin{aligned} &\int_{\mathcal{D}} \left(\left[\psi^T \delta w\right]_0^{t_f} - \int_0^{t_f} \frac{\partial \psi^T}{\partial t}\delta w dt \right) d\mathcal{D} \\ &+ \int_0^{t_f} \left[\int_{\mathcal{B}} n_k \psi^T \left(C_k \delta w + \delta S_{kl} f_l\right) d\mathcal{B} \right. \\ &- \left. \int_{\mathcal{D}} \frac{\partial \psi^T}{\partial \xi_k}\left(C_k \delta w + \delta S_{kl} f_l\right) d\mathcal{D} \right] dt = 0. \end{aligned}$$

Rearrange the terms in the equation

$$\begin{aligned} &\int_{\mathcal{D}} \left[\psi^T(t_f)\delta w(t_f) - \psi^T(0)\delta w(0) \right] d\mathcal{D} \\ &- \int_0^{t_f}\!\!\int_{\mathcal{D}} \frac{\partial \psi^T}{\partial t}\delta w + \frac{\partial \psi^T}{\partial \xi_k} C_k \delta w \, d\mathcal{D} dt \\ &+ \int_0^{t_f}\!\!\int_{\mathcal{B}} n_k \psi^T \delta F_k d\mathcal{B} + \int_0^{t_f} \left[\int_{\mathcal{B}} n_k \psi^T \delta S_{kl} f_l d\mathcal{B} \right. \\ &\left. - \int_{\mathcal{D}} \frac{\partial \psi^T}{\partial \xi_k}\delta S_{kl} f_l d\mathcal{D} \right] dt = 0. \end{aligned}$$

Since the left hand expression equals zero, it may be subtracted from the variation in the cost function (8) to give

$$\begin{aligned} \delta I &= \frac{1}{\frac{1}{2}\gamma P_\infty M_\infty^2 \bar{c}} \int_0^{t_f}\!\!\int_{\mathcal{B}_W} \delta p \left[\frac{\partial y}{\partial \xi}\cos\alpha - \frac{\partial x}{\partial \xi}\sin\alpha \right] \\ &\quad + p\left[\delta\left(\frac{\partial y}{\partial \xi}\right)\cos\alpha - \delta\left(\frac{\partial x}{\partial \xi}\right)\sin\alpha \right] d\xi dt \\ &\quad - \int_{\mathcal{D}} \left[\psi^T(t_f)\delta w(t_f) - \psi^T(0)\delta w(0) \right] d\mathcal{D} \\ &\quad + \int_0^{t_f}\!\!\int_{\mathcal{D}} \frac{\partial \psi^T}{\partial t}\delta w + \frac{\partial \psi^T}{\partial \xi_k} C_k \delta w \, d\mathcal{D} dt \\ &\quad - \int_0^{t_f}\!\!\int_{\mathcal{B}} n_k \psi^T \delta F_k d\mathcal{B} - \int_0^{t_f} \left[\int_{\mathcal{B}} n_k \psi^T \delta S_{kl} f_l d\mathcal{B} \right. \\ &\quad \left. + \int_{\mathcal{D}} \frac{\partial \psi^T}{\partial \xi_k}\delta S_{kl} f_l d\mathcal{D} \right] dt. \quad (9) \end{aligned}$$

Now, since ψ is an arbitrary differentiable function, it may be chosen in such a way that δI no longer depends explicitly on the variation of the state vector δw. The gradient of the cost function can then be evaluated directly from the metric variations without having to re-compute the variation δw resulting from the perturbation of each design variable. The variation δw can be eliminated from (9) to produce a differential adjoint system governing ψ

$$\frac{\partial \psi}{\partial t} + C_k^T \frac{\partial \psi}{\partial \xi_k} = 0 \quad \text{in D.} \quad (10)$$

At the outer boundary incoming characteristics for ψ correspond to outgoing characteristics for δw. Consequently we can choose boundary conditions for ψ such that

$$n_k \psi^T C_k \delta w = 0.$$

If the coordinate transformation is such that δS is negligible in the far field, then the only remaining

boundary terms is

$$-\int_{\mathcal{B}_W} \psi^T \delta F_2 d\xi_1.$$

Thus, by letting ψ satisfy the boundary condition,

$$\psi_j n_j = \frac{1}{\frac{1}{2}\gamma P_\infty M_\infty^2 \bar{c}} \left[\frac{\partial y}{\partial \xi}\cos\alpha - \frac{\partial x}{\partial \xi}\sin\alpha\right] \quad \text{on } \mathcal{B}_W \tag{11}$$

where n_j are the components of the surface normal. Since the initial condition for the Lagrange multipliers are set to zero, then

$$\psi^T(0)\delta w(0) = 0.$$

Since the cost function used for this problem is not dependent upon t_f, then

$$\psi^T(t_f)\delta w(t_f) = 0.$$

Equation (9) finally reduces to the following

$$\begin{aligned}\delta I &= \frac{1}{\frac{1}{2}\gamma P_\infty M_\infty^2 \bar{c}} \int_0^{t_f}\int_{\mathcal{B}_W} p\left[\delta\left(\frac{\partial y}{\partial \xi}\right)\cos\alpha \right. \\ &\left. -\delta\left(\frac{\partial x}{\partial \xi}\right)\sin\alpha\right] d\xi dt - \int_0^{t_f}\left[\int_{\mathcal{B}} n_k \psi^T \delta S_{kl} f_l d\mathcal{B} \right. \\ &\left. -\int_{\mathcal{D}} \frac{\partial \psi^T}{\partial \xi_k}\delta S_{kl} f_l d\mathcal{D}\right] dt. \end{aligned} \tag{12}$$

Derivation of the Time Accurate Discrete Unsteady Adjoint Equations for the Euler Equations

The unsteady discrete adjoint equation is obtained by applying control theory directly to the set of unsteady discrete field equations. The resulting equation depends on the type of scheme used to solve the flow equations. This paper uses a cell-centered multigrid-driven fully-implicit scheme with upwind-biased blended first and third order fluxes as the artificial dissipation scheme.

To obtain a fully-implicit algorithm, approximate (3) as

$$\frac{d}{dt}\left[w_{i,j}^{n+1}V_{i,j}^{n+1}\right] + R(w_{i,j}^{n+1}) = 0. \tag{13}$$

The time derivative term can be approximated by a kth-order implicit backward difference formula (BDF) such as,

$$\frac{d}{dt} = \frac{1}{\Delta t}\sum_{q=1}^{k}\frac{1}{q}\left[\Delta^-\right]^q, \tag{14}$$

where

$$\Delta^- = w_{i,j}^{n+1} - w_{i,j}^{n}.$$

A second order expansion of equation (14) will result to the following equation

$$\begin{aligned}&\frac{3}{2\Delta t}\left[w_{i,j}^{n+1}V_{i,j}^{n+1}\right] - \frac{2}{\Delta t}\left[w_{i,j}^{n}V_{i,j}^{n}\right] \\ &+\frac{1}{2\Delta t}\left[w_{i,j}^{n-1}V_{i,j}^{n-1}\right] + R(w_{i,j}^{n+1}) = 0.\end{aligned} \tag{15}$$

Equation (15) represents an implicit set of coupled ordinary differential equations and can be solved at each time step using the explicit multistage modified Runge-Kutta scheme. We define a new modified residual $R^*(w_{i,j})$ as

$$\begin{aligned}R^*(w_{i,j}) = &\frac{3}{2\Delta t}\left[w_{i,j}^{n+1}V_{i,j}^{n+1}\right] - \frac{2}{\Delta t}\left[w_{i,j}^{n}V_{i,j}^{n}\right] \\ &+\frac{1}{2\Delta t}\left[w_{i,j}^{n-1}V_{i,j}^{n-1}\right] + R(w_{i,j}^{n+1}).\end{aligned} \tag{16}$$

The modified residual is then marched to steady-state in a fictitious time, t^* as follows

$$\frac{dw_{i,j}}{dt^*} + R^*(w_{i,j}) = 0.$$

Take a variation of equation (16) with respect to the state vector, w and shape function, f (only terms that are multiplied to δw are shown)

$$\begin{aligned}\delta R_{i,j}^{*^{n+1}}(w) &= \frac{3}{2\Delta t}\left[\delta w_{i,j}^{n+1}V_{i,j}^{n+1}\right] - \frac{2}{\Delta t}\left[\delta w_{i,j}^{n}V_{i,j}^{n}\right] \\ &+ \frac{1}{2\Delta t}\left[\delta w_{i,j}^{n-1}V_{i,j}^{n-1}\right] + \delta R_{i,j}^{n+1}(w).\end{aligned} \tag{17}$$

Multiply the above equation with a Lagrange multiplier and integrate over the domain and time to yield

$$\begin{aligned}\sum_{t=0}^{t_f}\sum_{\Omega}\psi_{i,j}^T\delta R_{i,j}^*(w) &= \cdots + \psi_{i,j}^{T^{n+1}}\delta R_{i,j}^{*^{n+1}}(w) \\ &+\psi_{i,j}^{T^{n+2}}\delta R_{i,j}^{*^{n+2}}(w) + \psi_{i,j}^{T^{n+3}}\delta R_{i,j}^{*^{n+3}}(w) + \cdots\end{aligned}$$

Substitute equation (17) into the above equation to yield (only $n+1$ terms are shown)

$$\begin{aligned}&\sum_{t=0}^{t_f}\sum_{\Omega}\psi_{i,j}^T\delta R_{i,j}^*(w) = \\ &\cdots + \psi_{i,j}^{T^{n+1}}\left[\frac{3}{2\Delta t}V^{n+1}\delta w_{i,j}^{n+1} + \delta R_{i,j}^{n+1}\right] \\ &+\psi_{i,j}^{T^{n+2}}\left[-\frac{2}{\Delta t}V^{n+1}\delta w_{i,j}^{n+1}(w)\right] \\ &+\psi_{i,j}^{T^{n+3}}\left[\frac{1}{2\Delta t}V^{n+1}\delta w_{i,j}^{n+1}(w)\right] + \cdots\end{aligned}$$

Rearrange the terms in the equation to produce the

discrete time accurate unsteady adjoint equation

$$\sum_{t=0}^{t_f}\sum_{\Omega}\psi_{i,j}^{T}\delta R_{i,j}^{*}(w) = \cdots + [\frac{3}{2\Delta t}V^{n+1}\psi_{i,j}^{T^{n+1}} - \frac{2}{\Delta t}V^{n+1}\psi_{i,j}^{T^{n+2}} + \frac{1}{2\Delta t}V^{n+1}\psi_{i,j}^{T^{n+3}} + \psi_{i,j}^{T^{n+1}}\delta R_{i,j}^{n+1}]\delta w_{i,j}^{n+1}(w) + \cdots \quad (18)$$

Next we introduce the discrete cost function for the time average drag minimization problem as

$$\begin{aligned} I_c &= \sum_{t=0}^{t_f} C_d\,\Delta t = \sum_{t=0}^{t_f}\left(C_a\cos\alpha + C_n\sin\alpha\right)\Delta t \\ &= \frac{1}{\frac{1}{2}\gamma P_\infty M_\infty^2\,\bar{c}}\sum_{t=0}^{t_f}\sum_{\mathcal{B}_w} p_{i,W}\left(\frac{\Delta y_i}{\Delta s_i}\cos\alpha - \frac{\Delta x_i}{\Delta s_i}\sin\alpha\right)\Delta s_i\Delta t, \end{aligned}$$

where Δs_i is the cell arc length and $\Delta p_{i,W}$ is the wall pressure. A variation in the cost function will result to a variation, Δp, in the pressure and a variation, Δy and Δx, in the geometry. The variation of the cost function for drag minimization can be written as

$$\begin{aligned} \delta I_c &= \frac{1}{\frac{1}{2}\gamma P_\infty M_\infty^2\,\bar{c}}\sum_{t=0}^{t_f}\left[\sum_{\mathcal{B}_w}\left(\frac{\Delta y_i}{\Delta s_i}\cos\alpha - \frac{\Delta x_i}{\Delta s_i}\sin\alpha\right)\frac{\partial p}{\partial w}\delta w_{i,W}\Delta s_i + \sum_{\mathcal{B}_W}(p_{i,W}-p_\infty)\right. \\ &\quad \left.[\cos\alpha\;\delta\left(\Delta y_i\right) - \sin\alpha\;\delta\left(\Delta x_i\right)]\right]\Delta t. \end{aligned} \quad (19)$$

The time-dependent discrete Euler equations can now be introduced into δI as a constraint to produce

$$\delta I = \delta I_c - \sum_{t=0}^{t_f}\sum_{\Omega}\psi_{i,j}^{T}\delta R_{i,j}^{*}(w).$$

Substitute equation (18) and (19) into the above expression, which can then be rearranged into two main categories; first, terms that are multiplied by the variation of the state vector, δw, and second, terms that are multiplied to the variation of the shape function, δf.

The time-dependent discrete adjoint equation can now be defined as such

$$\frac{\partial\psi_{i,j}^{n+1}}{\partial\tau} - \left[\frac{3}{2\Delta t}\psi_{i,j}^{T^{n+1}} - \frac{2}{\Delta t}\psi_{i,j}^{T^{n+2}} + \frac{1}{2\Delta t}\psi_{i,j}^{T^{n+3}}\right]V^{n+1} - \psi_{i,j}^{T^{n+1}}\delta_w R_{i,j}^{n+1} = 0. \quad (20)$$

At cell $i,2$ the time-dependent discrete adjoint equation is as follows,

$$\begin{aligned} &\frac{\partial\psi_{i,2}^{n+1}}{\partial\tau} - \left[\frac{3}{2\Delta t}\psi_{i,j}^{T^{n+1}} - \frac{2}{\Delta t}\psi_{i,j}^{T^{n+2}} + \frac{1}{2\Delta t}\psi_{i,j}^{T^{n+3}}\right]V^{n+1} - \frac{1}{2}\left[A_{i-\frac{1}{2},2}^{T^{n+1}}\left(\psi_{i,2}^{n+1}-\psi_{i-1,2}^{n+1}\right)\right. \\ &+A_{i+\frac{1}{2},2}^{T^{n+1}}\left(\psi_{i+1,2}^{n+1}-\psi_{i,2}^{n+1}\right) \\ &\left.+B_{i,\frac{5}{2}}^{T^{n+1}}\left(\psi_{i,3}^{n+1}-\psi_{i,2}^{n+1}\right)-\Phi\right], \end{aligned} \quad (21)$$

where Φ is the source term for drag minimization,

$$\begin{aligned} \Phi &= \Delta y_\xi\psi_{2_{i,2}}^{n+1} - \Delta x_\xi\psi_{3_{i,2}}^{n+1} \\ &\quad + \left(\frac{\Delta y_i}{\Delta s_i}BCX - \frac{\Delta x_i}{\Delta s_i}BCY\right)\frac{\partial p}{\partial w}\Delta s_i\Delta t. \end{aligned} \quad (22)$$

where $BCX = BCD\cos\alpha$, $BCY = BCD\sin\alpha$, $BCD = \frac{1}{\frac{1}{2}\gamma P_\infty M_\infty^2\,\bar{c}}$. All the terms in equation (21) except for the source term are scaled as the square of the Δx. Therefore, as the mesh width is reduced, the terms in the source term if divided by Δs_i must approach zero as the solution reaches a steady state. One then recovers the continuous adjoint boundary condition as stated in equation (11). A full discretization of the equation would involve discretizing every term that is a function of the state vector. If a first order artificial dissipation equation is used, then the discrete adjoint equations are completely independent of the costate variables in the cells below the wall. However, if we use the blended first and third order equations, then these values are required.

Optimization Procedure

The search procedure used in this work is a simple descent method in which small steps are taken in the negative gradient direction. Let $\mathcal{F}$ represent the design variable, and $\mathcal{G}$ the gradient. An improvement can then be made with a shape change

$$\delta\mathcal{F} = -\lambda\mathcal{G}.$$

The gradient $\mathcal{G}$ can be replaced by a smoothed value $\overline{\mathcal{G}}$ in the descent process. This ensures that each new shape in the optimization sequence remains smooth and acts as a preconditioner which allows the use of much larger steps. To apply smoothing in the ξ_1 direction, the smoothed gradient $\overline{\mathcal{G}}$ may be calculated from a discrete approximation to

$$\overline{\mathcal{G}} - \frac{\partial}{\partial\xi_1}\epsilon\frac{\partial}{\partial\xi_1}\overline{\mathcal{G}} = \mathcal{G},$$

where ϵ is the smoothing parameter. If the modification is applied on the surface $\xi_2 =$ constant, then the first order change in the cost function is

$$
\begin{aligned}
\delta I &= -\int\int \mathcal{G}\delta\mathcal{F}d\xi_1 \\
&= -\lambda\int\int\left(\overline{\mathcal{G}} - \frac{\partial}{\partial\xi_1}\epsilon\frac{\partial}{\partial\xi_1}\overline{\mathcal{G}}\right)\overline{\mathcal{G}}d\xi_1 \\
&= -\lambda\int\int\left(\overline{\mathcal{G}}^2 + \epsilon\left(\frac{\partial\overline{\mathcal{G}}}{\partial\xi_1}\right)^2\right)d\xi_1 \\
&< 0,
\end{aligned}
$$

assuring an improvement if λ is sufficiently small and positive. The smoothing leads to a large reduction in the number of design iterations needed for convergence. An assessment of alternative search methods for a model problem is given by Jameson and Vassberg.[10]

Design Process

In this section, we describe the design process for the full unsteady design (unsteady-flow unsteady-adjoint), partial unsteady design (unsteady-flow steady-adjoint), time-averaged-flow steady adjoint, and multipoint approaches.

Full Unsteady Design
(Unsteady-Flow Unsteady-Adjoint)

The following steps detail the procedures for the full unsteady continuous and discrete based design optimization problem:

1. **Unsteady Flow Calculation**. All numerical simulations were computed for an inviscid flow using a fully implicit second order backward difference formula, a five stage modified Runge-Kutta time stepping scheme was employed at each time instance using a blended first and third order artificial dissipation scheme. A 5-level W-cycle multigrid and residual averaging were used to accelerate the convergence. Problems considered in this work involved the RAE 2822 and VR-7 airfoils undergoing a forced pitching oscillation about the quarter-chord. The angle of incidence is given by

   $$\alpha(t) = \alpha_o + \alpha_m \sin(\omega t),$$

   where $\alpha_o = 0^o$, $\alpha_m = 1.01^o$. In order to compute the entire unsteady flow solution, $\alpha(t)$ is divided into 24 discrete points or time instances. The fully implicit scheme described above is then employed to solve for the unsteady flow solution at each time instance. Generally, it requires five periods before a limit cycle is achieved. Here, a period refers to one full oscillation. During the last period, the flow solution at each time instance is saved in memory. 15 multigrid cycles were used for each time instance. If 24 time instances are used for each cycle and five cycles are used to achieve the limit cycle, then a total of 1800 multigrid cycles are required to obtain the unsteady solution.

2. **Perturb α_o to maintain time average lift coefficient**. In order to maintain the time average lift coefficient, the mean angle of attack, α_o, is perturbed. However, α_o, is only modified every three periods, since it requires at least three periods for the global coefficients such as time average lift and drag to converge. A total of 15 periods are needed instead of 5 to achieve the desired time average lift coefficient. This multiplies the total cost by three times.

3. **Unsteady Adjoint Calculation**. The unsteady adjoint equation, either the discrete or continuous version, requires integration in reverse time. The same numerical scheme employed to solve the unsteady flow is used here as well with minor adjustments in the code to allow integration in reverse time. Only three periods were needed before the limit cycle is achieved. 15 multigrid cycles are used for each time instance, which translates to a total of 1080 cycles to achieve a limit cycle for the adjoint equation.

4. **Calculate Gradient**. The gradient is an integral over time. During the last period of the unsteady adjoint solver, the gradient at each time instance is computed and added to the previous one. At the end of the last period, the complete gradient is available. The gradient is then smoothed using an implicit smoothing technique described in the previous section.

5. **Modify Airfoil Shape**. The airfoil shape is then modified in the direction of improvement using a simple descent method.

6. **Update Grid**. The internal grid is modified based on perturbations on the surface of the airfoil.

7. **Repeat Design Process**. The entire design process is repeated until the objective function converges. The problems in this work typically required between nine to twenty five design cycles. Each design cycle required 1800 multigrid cycles to compute the flow solution and 1080 cycles for the adjoint solution.

Partial Unsteady Design
(Unsteady-Flow Steady-Adjoint)

The design process for the partial unsteady design optimization problem follows that of the full unsteady optimization described above except for two differences. First, in step 3, instead of an unsteady adjoint

computation using the fully implicit scheme, only a steady adjoint computation is performed for all 24 time instances which is equivalent to one period of the oscillation instead of three periods used in the full unsteady optimization case. At each time instance to compute the adjoint solution, the respective unsteady flow solution is used to compute the Euler Jacobian matrices. This corresponds to a factor of three computational savings for each design cycle. Thus only 360 multigrid cycles are required. Second, the gradient is no longer a time average of the gradients from each time instance, but rather an average of the gradients from all the time instance.

Time-Averaged-Flow Steady-Adjoint Design

The design process for the time-averaged-flow steady design follows that of the partial unsteady design procedure described above, except for the following two important points. Here, after the flow cycle is complete (limit cycle is achieved), the time-averaged-flow solution is computed. Then a single steady adjoint computation is performed using the time-averaged-flow solution at the mean angle of attack position, only requiring 15 multigrid cycles. The magnitude of the steady adjoint residuals reduces by 3 orders of magnitude in 15 multigrid cycles. Based on previous work by Nadarajah et. al.,[1] only a reduction of three orders of magnitude in the adjoint solution is required to obtain accurate gradient values for the Euler equations. The gradient is calculated based upon the time-averaged-flow solution and the steady adjoint solution.

Multipoint Design

In the multipoint design approach, the unsteady flow and adjoint solvers are replaced with a steady flow and adjoint solver for each time instance. The gradient is an average of the gradients from each time instance. Since only one period is required for both the flow and adjoint solvers, then the total computational cost is 720 multigrid cycles.

Method	Euler	Adjoint	Cost
Multipoint	360	360	1
Time-Averaged	1800	15	2.5
Partial	1800	360	3
Full	1800	1080	4

Table 1 Comparison of Computational Cost (Multigrid Cycles) Between Four Design Approaches.

Table 1 illustrates a cost comparison between the various design approaches. "Time-Averaged" refers to the time-averaged-flow steady adjoint design approach, "Partial" refers to the unsteady-flow steady-adjoint, and "Full" refers to the unsteady-flow unsteady-adjoint. Here the middle two columns contain the total number of multigrid cycles used to compute the Euler and adjoint equations. The numbers in the last column signify the ratio of cost of one method with respect to the Multipoint approach. Using the full unsteady design approach requires four times the computational cost as doing the multipoint approach. The difference in cost between one steady Runge-Kutta iteration and one unsteady Runge-Kutta iteration was not factored into the computing cost for each design approach, since the difference is minimal requiring only the addition of the time derivatives of the flow variables for the implicit time stepping for the unsteady algorithm.

Results

The following subsections present results of the time-averaged drag minimization problem for a two-dimensional airfoil undergoing a periodic pitching motion. The first subsection contains a code and grid validation study. The second subsection is dedicated to the redesign of the RAE 2822 airfoil to reduce the time-averaged drag coefficient while maintaining the time-averaged lift coefficient. The third section contains results of the time-averaged drag minimization of a VR-7 advanced rotorcraft airfoil. A comparison of a multipoint design, time-averaged flow steady-adjoint, partial unsteady, and a full unsteady design is explored in the last subsection.

Code and Grid Validation

Six computational grids are used in the grid validation study. Table 2 provides a list of the six different grids. The lens-mesh grids were generated using a hyperbolic grid generator. Figure 1 illustrates the full 193x33 mesh and a close up view of the NACA 64A010. There are 129 points on the surface of the airfoil.

Grid	Dimensions
Coarse 1	193x33
Coarse 2	193x65
Medium 1	257x33
Medium 2	257x65
Fine 1	321x33
Fine 2	321x65

Table 2 Euler Lens-Mesh Descriptions

Euler solutions were then computed for each grid and the lift coefficient versus angle of attack was compared with the experimental NACA 64A010 CT6[8] data. Here the computations were performed at a freestream Mach number, $M_\infty = 0.78$, at a mean angle of attack, $\alpha_o = 0^o$, and at a reduced frequency, $\omega_r = 0.202$. Five cycles of computation were required to allow the time-averaged lift and drag coefficients to converge. Figure 2 illustrates the hysteresis loop for all six grids and the CT6 experimental results. The results were relatively independent of the grid size and reproduced the experimental results with sufficient accuracy.

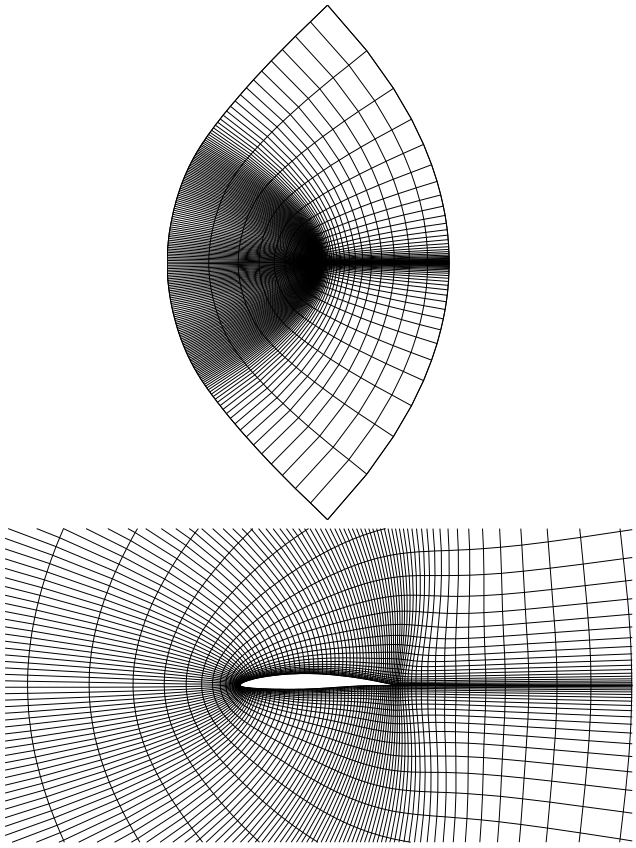

Fig. 1 Lens-Mesh 192x32: NACA 64A010

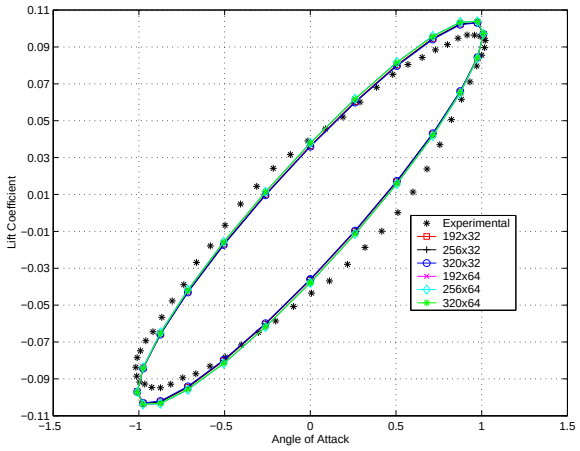

Fig. 2 Comparison of Lift Coefficient versus Angle of Attack for Various Lens-Mesh Grids and Experimental Results on a NACA 64A010 CT6 Case.

Since the primary objective of this paper is to formulate the unsteady discrete and continuous inviscid adjoint equations and prove their usefulness, numerical simulations and redesign computations in the upcoming subsections will only use the "Coarse 1" grid with 193x33 grid points, since its solutions are within acceptable accuracy.

In figure 3 we show the convergence history for the steady adjoint, unsteady continuous adjoint, and unsteady discrete adjoint equations. A cell-centered five

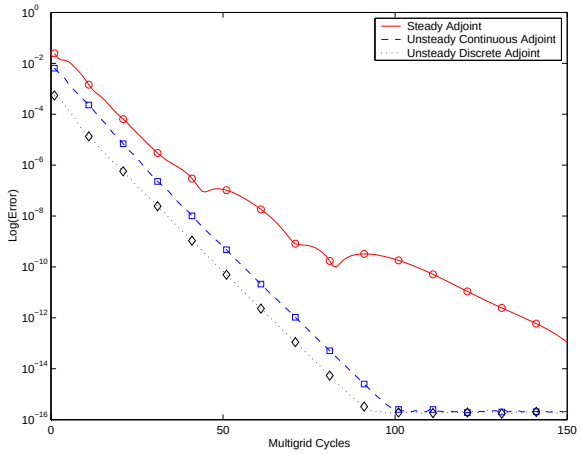

Fig. 3 Convergence History of the Steady, Unsteady Continuous, and Unsteady Discrete Adjoint Equations. 193x33 Lens-Mesh. RAE 2822 Airfoil, $M_\infty = 0.78$, $\omega_r = 0.202$, $\alpha_o = 0^o$

level W-cycle multigrid-driven fully-implicit scheme with upwind-biased blended first and third order fluxes as the artificial dissipation scheme were used for the unsteady continuous and discrete adjoint equations. An explicit multistage Runge-Kutta scheme was used to solve the equation at each time step. The continuous and discrete unsteady adjoint equations have the same convergence rate. The equations were solved for a RAE 2822 airfoil at Mach 0.78, $\alpha_o = 0^o$, and at a reduced frequency, $\omega_r = 0.202$ on a 193x33 lens-mesh.

RAE 2822: Time-Averaged Drag Minimization with Fixed Time-Averaged Lift Coefficient

Figure 4 illustrates the initial and final geometry for the RAE 2822 airfoil. The solid line represents the initial airfoil geometry and the dashed-line illustrates the redesigned airfoil. A distinctive feature of the new airfoil is in the drastic reduction of the upper surface curvature. A reduced curvature leads to a weaker shock and thus a lower wave drag, however, it also leads to a reduction in airfoil camber, resulting to a loss in lift. This effect is desirable for an advancing helicopter rotor blade since it operates at approximately zero lift but undesirable during the retreating phase, since the reduction in camber would reduce the $c_{l_{max}}$ and thus reduce the flight envelope, placing a limit on the forward flight speed.

In order to maintain the time-averaged lift coefficient, TAc_l, the mean angle of attack, α_o, is perturbed to a new value. The impact of this decision resulted to a need to compute more cycles to allow the TAc_l and TAc_d to converge. In this work, α_o was perturbed every three cycles. This allowed the TAc_l to converge to a new value before the angle of attack was perturbed any further. A total of 15 complete flow oscillation cycles were used for each design cycle. In figure 5 we show the initial and final lift coefficient hysteresis loops. The results show that to maintain the time-

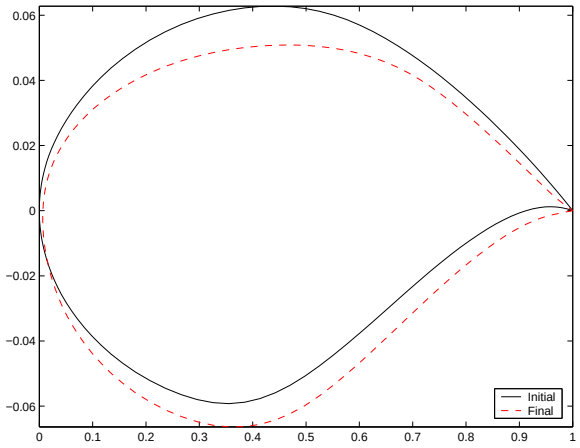

Fig. 4 Initial and Final Geometry for a RAE 2822 Airfoil at $M_\infty = 0.78$, $\omega_r = 0.202$, $\alpha_o = 0^o$

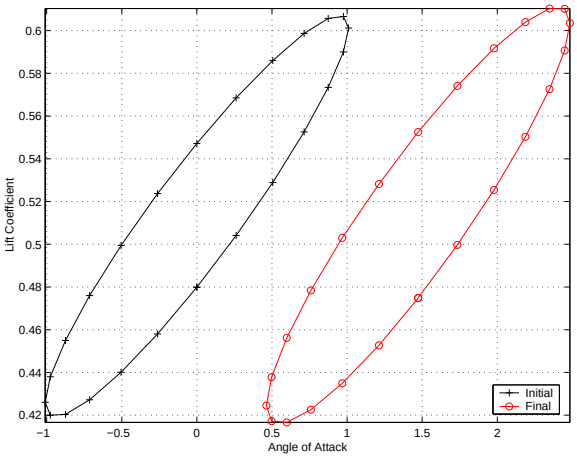

Fig. 5 Initial and Final Lift Coefficient Versus Angle of Attack for a RAE 2822 Airfoil at $M_\infty = 0.78$, $\omega_r = 0.202$, $\alpha_o = 0^o$

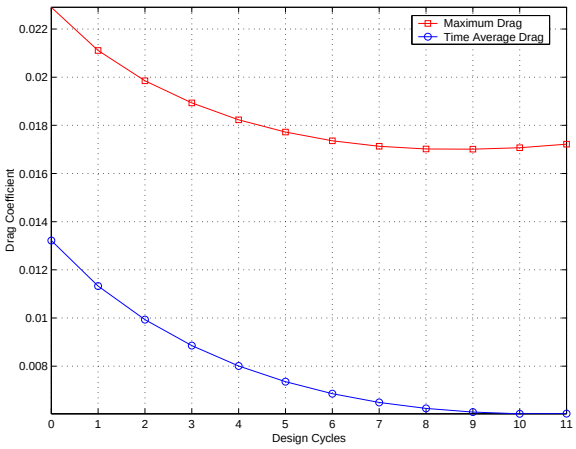

Fig. 6 Convergence of the Maximum and Time-Averaged Drag Coefficients for the RAE 2822 Airfoil at $M_\infty = 0.78$, $\omega_r = 0.202$, $\alpha_o = 0^o$

averaged lift coefficient, the mean angle of attack of the new airfoil increased by approximately 1.5 degrees. Figure 6 illustrates the convergence rate of the objective function: TAc_d. The TAc_d reduces by 53% from 132 drag counts to 62 drag counts within 11 design cycles. The maximum drag, however, reduces by only 25% from 229 drag counts to 172 drag counts.

Figures 7(a-d) illustrate the upper and lower surface instantaneous pressure coefficients for the initial and final design. In figures 7(a-b), a comparison of the initial instantaneous pressure distribution versus the final at 0^o phase shows an almost complete reduction of the wave drag. The strong shock on the suction side of the airfoil is weakened at all other phases of the oscillation.

Figures 8(a-b) show the pressure contour for the initial and final airfoil at 0^o. The sonic line represented by a dashed line is over-plotted on each figure. It is clearly visible that the strong shock on the upper surface of the initial geometry has been almost completely eliminated. However, a supersonic zone still exists. Here the air velocity is accelerated to a supersonic speed and gradually recovers to the freestream pressure at the trailing edge without a shockwave.

VR-7: Time-Averaged Drag Minimization with Fixed Time-Averaged Lift Coefficient

The VR-7 rotor profile is part of a family of advanced rotor airfoils designed by Leo Dadone[11] at Boeing. The VR-7 (t/c=0.12) and the VR-8 (t/c=0.08) were designed for the rotors on the Heavy lift Helicopter (HLH)- in 1971. The VR-7 profile is used up to the 85% span location of the blade and VR-8 is used at the tip. According to Dadone, the blade profile between the 85% and 99% span locations were obtained by interpolating between the VR-7 and VR-8. The airfoil was designed to have a very low pitching moment coefficient at zero angle of attack to maintain the oscillatory load level of the control system and high maximum lift coefficient.

Figure 9 illustrates the initial and final geometry for the VR-7 airfoil. The solid line represents the initial airfoil geometry and the dashed-line illustrates the redesigned airfoil. Similar to the redesigned RAE 2822, the upper surface curvature of the VR-7 advanced helicopter rotor has reduced as well. Figure 10 illustrates the convergence rate of the objective function: TAc_d. The TAc_d reduces by 22% from 309 drag counts to 240 drag counts within 25 design cycles.

Multipoint Versus Unsteady Optimization

Often a multipoint design approach has been the method of choice for optimization of airfoils in an unsteady flow environment due to its lower computational and memory cost. In this subsection of the paper, we make the argument that even if a multipoint design approach is cheaper, it cannot replace a full unsteady optimization. The following results will show that there are benefits to unsteady optimization.

In order to compare the multipoint design approach

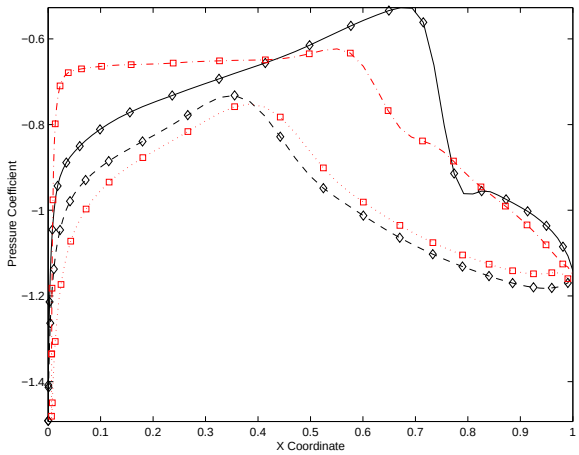

6(a) Phase = 0 degrees

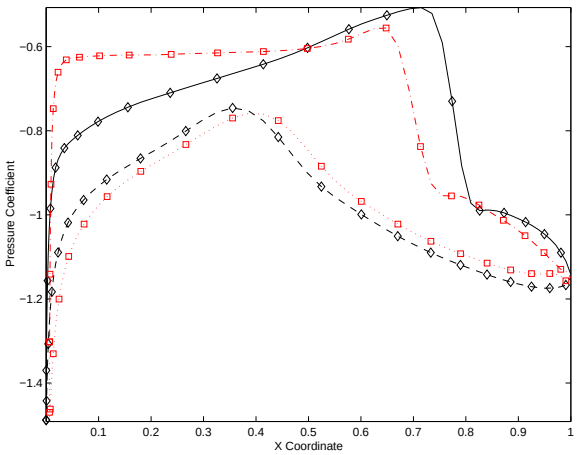

6(c) Phase = 180 degrees

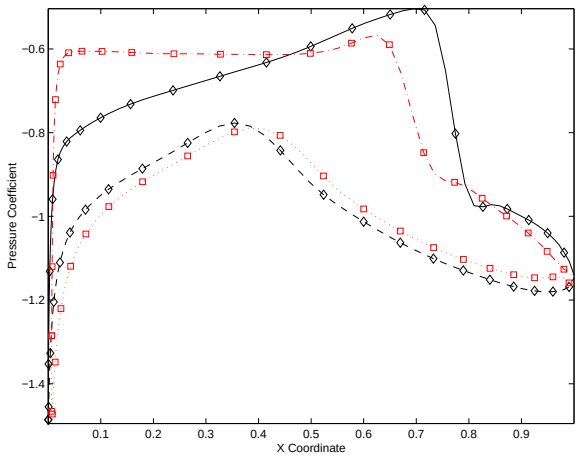

6(b) Phase = 90 degrees

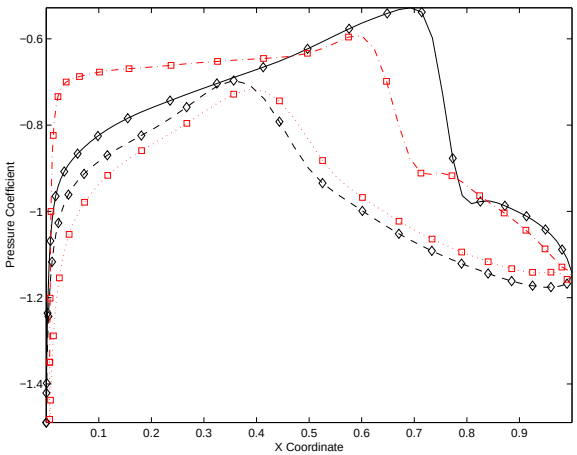

6(d) Phase = 270 degrees

Fig. 7 Convergence of the Maximum and Time-Averaged Drag Coefficients for the RAE 2822 a $M_\infty = 0.78$, $\omega_r = 0.202$, $\alpha_o = 0^o$ (-◇-): Initial Pressure, (−□−): Final Pressure

to the full unsteady optimization, several unsteady design cases were tested for various reduced frequencies. It is expected that at very low reduced frequencies, the flow characteristics are very similar to that of steady state computations. Full unsteady design cases were computed for reduced frequencies ranging from 0.050 to 0.450 at a Mach number, $M_\infty = 0.78$. The time average lift coefficient for all reduced frequencies were fixed to the same value of $TAc_l = 0.51$.

Next, the time-averaged-flow steady-adjoint and the partial unsteady design approaches were used to optimize the RAE 2822 airfoil at the flow conditions described above. Optimizations were only computed at a reduced frequency of 0.450.

Figure 11 illustrates a comparison of the airfoil geometries between the initial airfoil, airfoils designed at various reduced frequencies, and airfoil designed using the multipoint approach. The airfoils were designed at a Mach number, $M_\infty = 0.78$, at a mean angle of attack, $\alpha_o = 0^o$, and an angle of attack deviation of $\pm 1.01^o$. We show in figure 11 that the airfoil designed using the multipoint approach is almost identical to the one designed using a full unsteady optimization approach at a reduced frequency of $\omega_r = 0.050$. Figure 12 further supports this fact with an identical (within the numerical accuracy of the code) final time-averaged drag coefficient of 80 drag counts. Airfoils designed using the time-averaged-flow steady-adjoint and the partial unsteady design approaches are not shown in figure 11 since they are almost identical to the airfoil designed using the full unsteady optimization approach at a reduced frequency of 0.450.

The difference in the final airfoil geometry between designs performed at various reduced frequencies are very small except in areas on the upper surface where a greater reduction in the curvature is seen for higher reduced frequencies. Table 3 contains a comparison of the initial and final time-averaged drag coefficients for the various design approaches performed at various reduced frequencies. The design computations for the full unsteady optimization were executed at reduced frequencies: 0.050, 0.100, 0.150, 0.202, 0.250, 0.300, 0.350, 0.400, and 0.450. The convergence of the objective function (time-averaged drag) for design cases

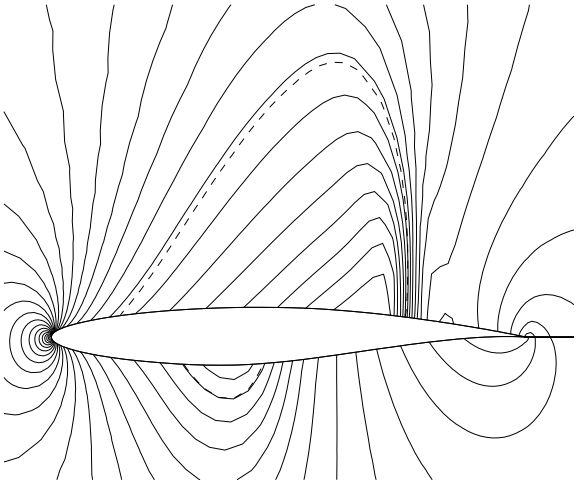

7(a) Initial Airfoil: Phase = 0^o

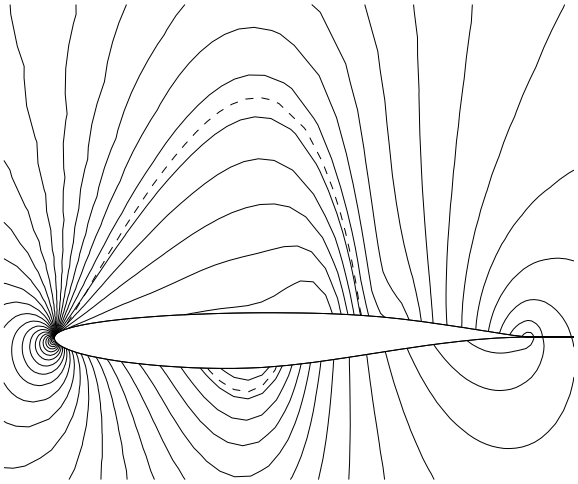

7(b) Final Design: Phase = 0^o

Fig. 8 Pressure Contour Plot for RAE 2822 Airfoil. Grid - 192 x 32, $M_\infty = 0.78$, $\omega_r = 0.202$, Fixed $C_l = 0.534$

with reduced frequencies higher than 0.400 resulted to the same answer. Therefore the three unsteady cases showcased in table 3 and figures 11 and 12 represent the lower limit, middle, and upper limit of the reduced frequency range. This simple example shows that a full unsteady optimization has a large benefit.

Case	Ini_{TAc_d}	Final_{TAc_d}	Reduction
Full $\text{Unst.}_{0.050}$	139	80	42%
Full $\text{Unst.}_{0.202}$	132	62	53%
Full $\text{Unst.}_{0.450}$	132	57	56%
Partial $\text{Unst.}_{0.450}$	132	58	56%
TA-Flow $\text{Steady}_{0.450}$	132	58	56%
Multipoint	146	82	43%

Table 3 Initial and Final Time-Averaged Drag Coefficient for Various Design Approaches

Since the design computation calculated at a reduced frequency of 0.450 using the full unsteady optimization approach produced the airfoil with the lowest time-averaged drag coefficient, we felt that this would be the best case to be compared with the time-averaged-flow steady adjoint and partial unsteady design approaches. Figure 12 illustrates that the history of the time-averaged drag coefficient is almost identical between the three design approaches. The results vary by only at most two drag counts at each design cycle. In figure 13 the gradients computed using the full continuous and discrete unsteady adjoint methods are compared to gradients computed using the time-averaged-flow steady adjoint and partial unsteady approaches. These gradients were computed after the first design cycle. There is an identical match between the full continuous and discrete unsteady adjoint methods. The time-averaged-flow steady adjoint gradient agree very well with the full and partial unsteady adjoint gradients. The sharp peak at grid point 115 illustrates the large gradient values close to the location of the shock wave. At this grid location, the partial unsteady and time-averaged-flow steady adjoint gradients have better agreement.

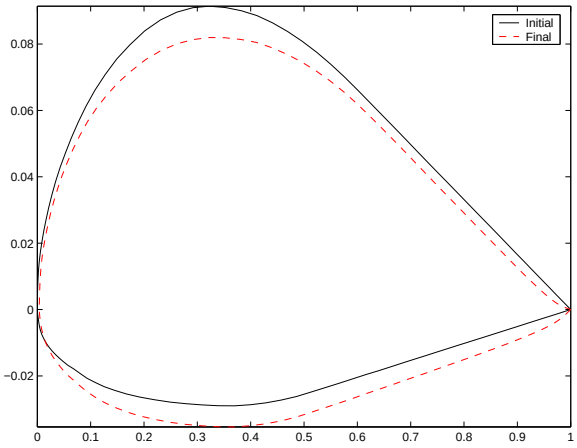

Fig. 9 Initial and Final Geometry for a VR-7 Airfoil at $M_\infty = 0.75$, $\omega_r = 0.202$, $\alpha_o = 0^o$

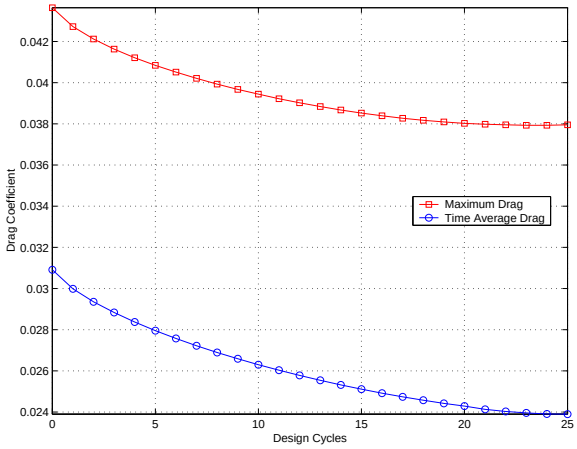

Fig. 10 Convergence of the Maximum and Time-Averaged Drag Coefficients for the VR-7 at $M_\infty = 0.75$, $\omega_r = 0.202$, $\alpha_o = 0^o$

Conclusion

This paper presents a complete formulation of the continuous and discrete unsteady inviscid adjoint approaches to automatic aerodynamic design. A 57% reduction in the time-averaged drag coefficient was achieved for the RAE 2822 airfoil at a reduced frequency of 0.450 while maintaining the time-averaged lift coefficient. The results also show that there are large benefits to modeling the unsteady flow. A comparison of the gradients produced by the time-averaged-flow steady adjoint, partial unsteady, and full unsteady adjoint illustrate that the gradients are not sensitive to the method by which the adjoint equations are modeled for the pitching airfoil problem used in this work. The framework has been established to extend this method to viscous dominated flows where secondary flow effects are present.

Acknowledgments

This research has benefited greatly from the generous support of the AFOSR under grant number AF F49620-98-1-022 and the Department of Energy under contract number LLNL B341491 as part of the Accelerated Strategic Computing Initiative (ASCI) program.

References

[1]S. Nadarajah and A. Jameson Studies of the Continuous and Discrete Adjoint Approaches to Viscous Automatic Aerodynamic Shape Optimization. *AIAA 2001-2530*, 15th AIAA Computational Fluid Dynamics Conference, Anaheim, CA, June 2001.

[2]S. Nadarajah, A. Jameson, and J. Alonso An Adjoint Method for the Calculation of Remote Sensitivities in Supersonic Flow. *AIAA 2002-0261*, 40th AIAA Aerospace Sciences Meeting and Exhibit, Reno, NV, January 2002.

[3]P. G. Wilby. Shockwaves in the rotor world – a personal perspective of 30 years of rotor aerodynamic developments in the UK. In *The Aeronautical Journal*, 113-128, March 1998.

[4]A. Jameson. Time Dependent Calculations using Multigrid, with Applications to Unsteady Flows Past Airfoils and Wings. *AIAA 91-1596*, AIAA 10th Computational Fluid Dynamics Conference, Honolulu, HI, June 1991.

[5]K. Ghayour and O. Baysal Unsteady Aerodynamics and Shape Optimization using Modified Transonic Small Disturbance Equation. *AIAA 99-0654*, 37th AIAA Aerospace Sciences Meeting and Exhibit, Reno, NV, January 1999.

[6]K. Yee, Y. Kim, and D. Lee Aerodynamic Shape Optimization of Rotor Airfoils Undergoing Unsteady Motion. *AIAA 99-3107*, 37th AIAA Aerospace Sciences Meeting and Exhibit, Reno, NV, January 1999.

[7]R. Florea and K. C. Hall Sensitivity Analysis of Unsteady Inviscid Flow through Turbomachinery Cascades. *AIAA 2000-0130*, 38th AIAA Aerospace Sciences Meeting and Exhibit, Reno, NV, January 2000.

[8]S.S. Davis. NACA 64A010 (NASA Ames Model) Oscillatory Pitching. *AGARD Report 702*, AGARD, January 1982.

[9]A. Jameson. Solution of the Euler Equations for Two Dimensional Transonic Flow By a Multigrid Method. *Applied Mathematics and Computation*, 13:327-355, 1983.

[10]J. Vassberg and A. Jameson. Studies of Alternative Numerical Optimization Methods Applied to the Brachistochrone Problem.

[11]L. Dadone. Personal Communications on Advanced Rotor Blade Profiles.

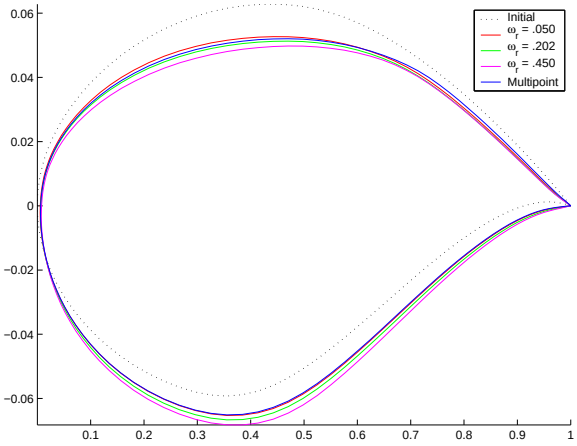

Fig. 11 A Comparison of Final Airfoil Geometries Between the Initial Airfoil, Airfoils Designed at Various Reduced Frequencies, and Airfoil Designed using the Multipoint Approach. $M_\infty = 0.78$, $\alpha_o = 0^o$, **Fixed** $C_l = 0.51$

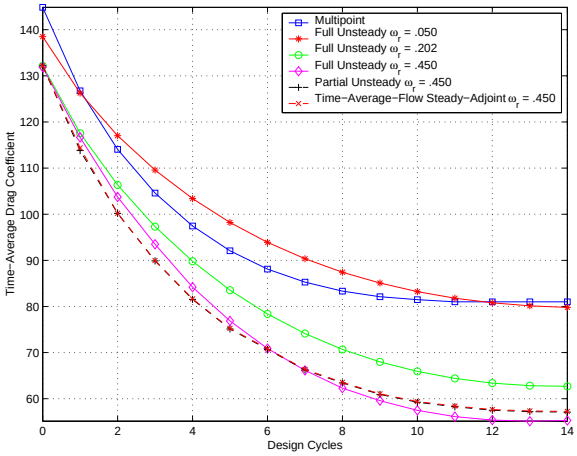

Fig. 12 Convergence History of the Time-Averaged Drag Coefficient for Various Design Approaches for the RAE 2822 Airfoil at $M_\infty = 0.78$, $\alpha_o = 0^o$, **Fixed** $C_l = 0.51$

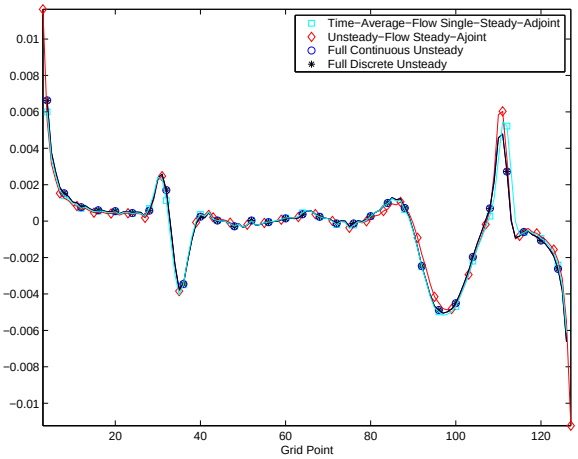

Fig. 13 Comparison of Time-Averaged-Flow Steady-Adjoint, Partial Unsteady, Full Continuous and Discrete Unsteady Gradients. RAE 2822 Airfoil, $M_\infty = 0.78$, $\alpha_o = 0^o$, **Fixed** $C_l = 0.51$